Collective nonlinear electric polarization via defect-driven local symmetry breaking

Wen Dong[1,2], David Cortie[1,3,4,*], Teng Lu[1], Qingbo Sun[1], Narendirakumar Narayanan[1,3], Wanbiao Hu[1], Lilit Jacob[5], Qian Li[6], Dehong Yu[3], Hua Chen[7], Aiping Chen[8], Xiaoyong Wei[9], Genmiao Wang[1], Mark G. Humphrey[1], Terry J. Frankcombe[5,*] and Yun Liu[1,*]

[1] Research School of Chemistry, The Australian National University, ACT 2601, Australia.

[2] Department of Physics, University of Warwick, Gibbet Hill Road, Coventry CV4 7AL, UK.

[3] Australia Nuclear Science and Technology Organisation, Lucas Height, NSW 2234, Australia.

[4] Institute for Superconducting and Electronic Materials, University of Wollongong, Innovation Campus, Squires Way, North Wollongong, NSW 2500, Australia.

[5] School of Physical, Environmental and Mathematical Sciences, The University of New South Wales, Canberra, ACT 2601, Australia.

[6] Advanced Photon Source Facility, Argonne National Laboratory, Lemont, IL 60439, USA.

[7] Centre for Advanced Microscopy, The Australian National University, ACT 2601, Australia

[8] Center for Integrated Nanotechnologies (CINT), Los Alamos National Laboratory, Los Alamos, NM 87545, USA.

[9] Electronic Materials Research Laboratory, Key Laboratory of the Ministry of Education & International Center for Dielectric Research, Xi'an Jiaotong University, Xi'an, 710049, China

*To whom the correspondence should be addressed: dcortie@uow.edu.au, t.frankcombe@adfa.edu.au and yun.liu@anu.edu.au

Abstract

In this work, we report the defect-mediated，abnormal non-linear polarization behavior observed in centrosymmetric rutile TiO_2 where less than 1 at% of sterically mismatched Mg^{2+} ions are introduced to create ferroelectric-like polarization hysteresis loops. It is found that the Mg''_{Ti}-$V_O^{\bullet\bullet}$ defect cluster produces a dipole moment exceeding 6 Debye, with a rotatable component. Such a polarization is further enhanced by the displacement of neighboring Ti^{4+} ions. The coupling between such defect-driven symmetry-breaking regions

generates a collective nonlinear electrical polarization state that persists to high temperatures. More importantly, an observation of abnormal bias shift of polarization hysteresis suggests an antiparallel alignment of certain dipoles frozen relative to the external poling electric field, which is associated with oxygen vacancy hopping. This result challenges the long-standing notion of parallel alignment of dipoles with the external electric field in ferroelectrics. The work also reveals an unexpected new form of non-linear dielectric polarization (non-ferroelectricity) in solid-state materials.

Introducing dopants into host materials is a common approach to modify the properties[1-4]. Often the strategy for choosing the dopants is based on the similarities between the dopants and host ions' size and electronegativity, which can only tune and modify the property of host materials to a certain extent. Recently, we found that the alternative concept of using "difficult-to-dope" ions, i.e., sterically-mismatched dopants that introduce structural frustration, can be a powerful strategy to tremendously alter the chemical environment and associated local structure surrounding the dopant/s, and thus significantly changing the property of host materials and even creating new functionalities[3, 5, 6]. This has been exemplified by the development of colossal permittivity materials in TiO_2-based materials[3, 7-11], and other metal oxides[12-15], where the co-doping ions (including one "difficult-to-dope" ion) are synergistically introduced into the host materials to form specific and large defect clusters[3] at equilibrium states to generate electron-pinned defect-dipoles. This defect design strategy is also used to prepare N-containing TiO_2 (N being a "difficult-to-dope" ion), where the cation-anion defect pairs are formed for highly-efficient visible light catalysis[6].

Such a defect-driven geometry frustration very often leads to spontaneous local symmetry breaking in materials[16], and subsequently affects the properties if this defect-induced interaction is sufficiently strong or acts over a large enough region. In either case, the overall average structure remains unchanged, but the properties are rather different. For example, Ren et al.[1] reported that oxygen vacancy would mediate polarization change and enhance piezoelectric property in cubic $BaTiO_3$, and Sala et al.[17] demonstrated that a low concentration of oxygen vacancy defects in pyrochlores could induce a magnetic distortion that markedly slows the long time monopole dynamics.

In this work, we deliberately introduce a small amount (0.025 at%~0.5 at%) of "difficult-to-dope" Mg^{2+} ions into the centrosymmetric rutile TiO_2. The Mg^{2+} ion is bigger than the Ti^{4+} ion, with the ionic radii being 86 pm and 75 pm,[18] respectively. Correspondingly, bond valance sums show that Mg^{2+} is significantly over-bonded when replacing Ti^{4+} ions (by 31%) unless one of six neighboring oxygens is removed from the structure.[19] The formation of Mg''_{Ti}-$V_O^{\bullet\bullet}$ pairs, on the other hand, results in structural frustration for the remaining nearby oxygen anions. The chemical environment surrounding these tightly-bound defect pairs is altered, leading to corresponding local structural symmetry breaking and subsequently change in physical properties. Here we systematically investigate the impact of Mg doping on electrical polarization behaviors. It is found that with less than 1 at% doping level of Mg^{2+} ions (where the doping level would determine the numbers of $Mg''_{Ti} - V_O^{\bullet\bullet}$ pairs when the materials were synthesized and reached equilibrant states), the electric polarization of TiO_2 is altered from linear to nonlinear, accompanied by an unusual poling anomaly that is unlike normal ferroelectric materials and some defect-induced ferroelectricity, such as doped HfO_2.[20-22] and (Nb, Al) co-doped TiO_2.[23] An associated theoretical model is also developed in this work to interpret the underlying mechanism behind these phenomena.

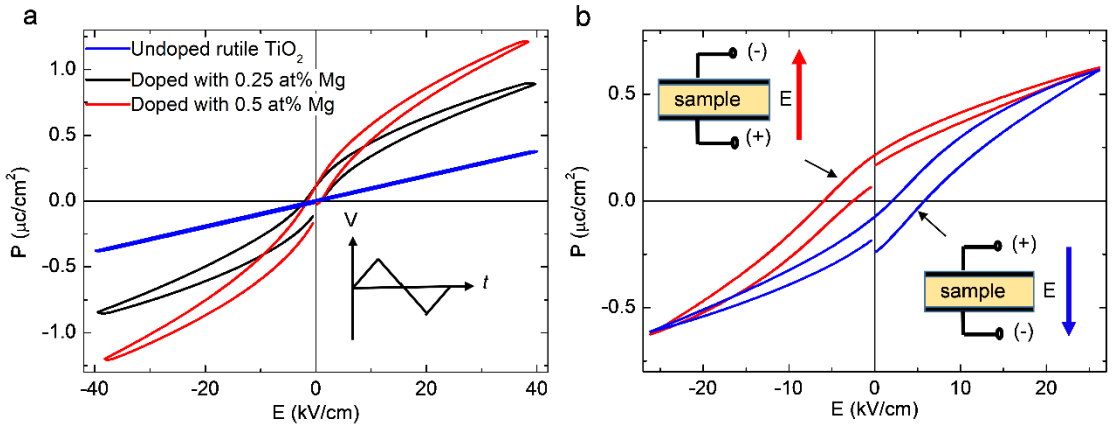

Fig. 1 Nonlinear electric polarization behavior of Mg doped rutile TiO_2. **a** Room temperature polarization-electric field (P-E) loop of pure (blue), fresh 0.25 at% (black) and 0.5 at% (red) Mg-doped rutile TiO_2, measured at 0.5 Hz without pre-poling. The inset shows the waveform of the applied electric field. This clearly indicates defect-driven linear-nonlinear polarization transition occurred in rutile TiO_2. **b** P-E loops of 0.25 at% Mg doped rutile TiO_2 collected after poling with a negative electric field E (red) and a relatively positive electric field (blue). A poling electric field

of 2.5 kV/cm was applied for a certain time on the sample at room temperature. The polarization hysteresis loop was measured by following the exactly same set up as shown in (**a**), where a triangle form of the electric field with a frequency of 10 Hz is used.

Nonstoichiometric rutile TiO_2 materials doped with Mg^{2+} ions, i.e. with a nominal composition $Mg_xTi_{1-x}O_{2-\delta}$ (x= 0.25 at%, 0.5 at%, 1 at% and 5 at%) were prepared by a conventional solid-state reaction route. Both X-ray diffraction (XRD) and scanning electron microscopy (SEM) analysis suggest Mg^{2+} ions (Figure S1-S3) with the doping level at least up to x = 0.5 at% are soluble and homogeneously distributed in rutile TiO_2, while its centrosymmetric $P4_2/mnm$ average structure still remains, in a good agreement with the results reported previously[24, 25]. No second-harmonic generation (SHG) effect is found, which further confirms the absence of average structure symmetry breaking in these samples. Electron paramagnetic resonance (EPR) characterization suggests that neither Ti^{3+} ion nor $V_O^{\bullet}$ are detectable in the materials (Figure S4 and associated detailed analysis). Therefore, there are only Mg^{2+}, Ti^{4+}, O^{2-} and $V_O^{\bullet\bullet}$ to be considered in Mg-doped TiO_2.

Fig. 1 presents the electric polarization (P) of pure and Mg-doped rutile TiO_2 (fresh sample) with respect to electric field (E) measured at 0.5 Hz. It is not surprising to see a linear polarization behavior in pure rutile TiO_2. Strikingly, Mg-doped TiO_2 samples exhibit a typical "ferroelectric-like" nonlinear P-E loop, although the value of spontaneous polarization is quite small, by contrast to normal ferroelectricity in conventional ferroelectric materials. The maximum polarization increases nearly proportionally with the increasing doping level, but the corresponding switching field (corresponding to the "coercive field" presented in the ferroelectric polarization hysteresis loop) is almost unchanged. It is found that the polarization increases with an increasing applied electric field, but the switching field remains almost unchanged when the applied maximum field doubles from 25 kV/cm to 50 kV/cm (Figure S5) and the switching field slightly increases with the increasing frequency of the electric field (Figure S6). Furthermore, there is no switchable domain image observed by the piezoresponse force microscopy. These results point to an abnormal nonlinear polarization hysteresis behavior being present in Mg-doped TiO_2, however, it is not ferroelectric.

Imitating the poling process applied in ferroelectric materials, a bias is applied on the fresh samples at room temperature for poling and then their P-E loops are measured. Surprisingly it is found (Fig.

1b) that an internal field is established during the poling process and the whole P-E loop is laterally shifted away from the origin where the P-E loop of the fresh doped samples is centered, analogous to the shifted hysteresis loop known as exchange bias in magnetic materials, which is associated with exchange anisotropy[26]. Most importantly, the respective direction of the internal field is the same as that of the externally applied electric field, i.e. the positive poling leads to the right shift of the P-E loop and vice versa. Increasing the temperature can reduce such an internal field and return to the fresh state once the temperature reaches to a certain value (Figure S7). It is also found that the electric-field-cycling leads to relaxation of the internal field and the P-E loop shifts back to the origin after the electric-field cycled over 10^5 times (Figure S8). This indicates that such an internal field built in Mg-doped rutile TiO_2 is metastable. The abnormal poling induced hysteresis behavior further confirm the that this not a ferroelectric behavior.

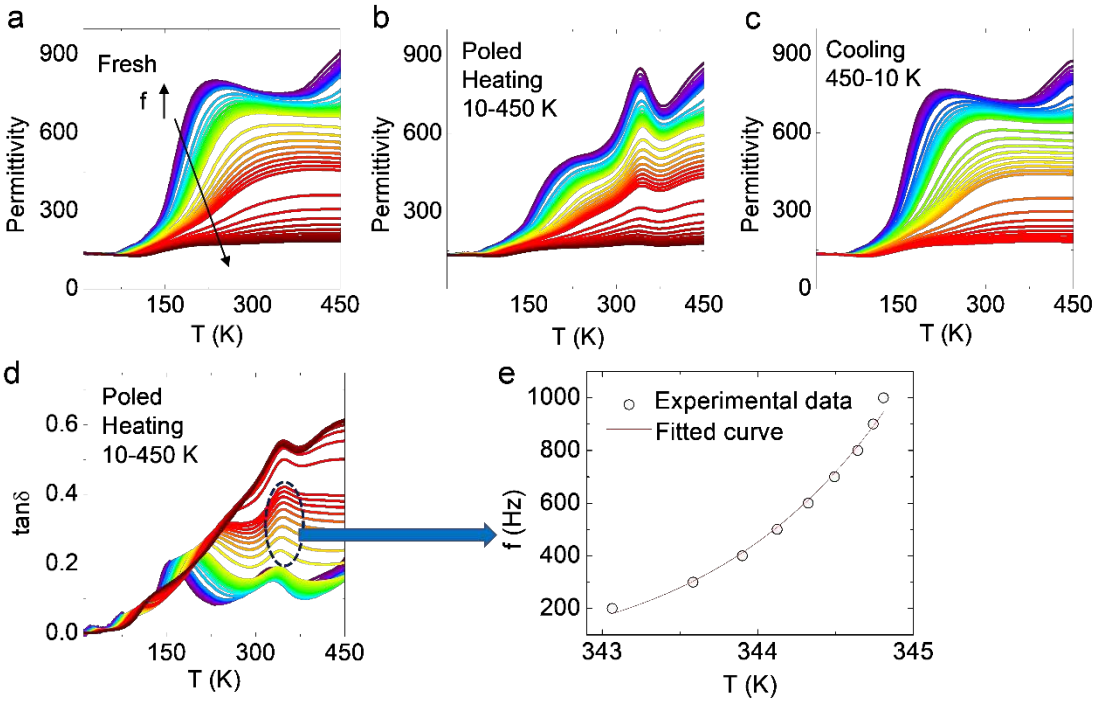

Fig. 2 Temperature-dependent dielectric permittivity of 0.25 at% Mg doped rutile TiO_2. The fresh (unpoled) (**a**) and poled (**b**, **c**) samples were measured from 20 Hz to 1 MHz in the temperature range of 10 K - 450 K. A negative electric field of 2.5 kV/cm is applied for poling at room temperature. **d** shows the temperature-dependent dielectric loss spectra related to (**b**). **e** is a fitting curve [Equation (1)] based on the relationship between the frequency and associated temperature

that corresponds to the peak of dielectric loss at this frequency. The experimental data in (**e**) were collected from the section circled by the dashed line in part (**d**).

To understand the nonlinear polarization behaviors observed in Mg-doped TiO_2, we investigated the temperature-dependent dielectric polarization behavior of the fresh and poled 0.25 at% Mg doped rutile TiO_2, especially paying attention to the data collected on heating and cooling. For fresh samples, there is no difference in their dielectric spectra between heating and cooling (Fig. 2a). The relaxation peak above 150 K can be well fitted using a Debye-derivative Havriliak-Negami relaxation model[27] with an activation energy of 0.196 eV. For poled samples, however, there is an additional relaxation peak that appears around 320 K during heating (Fig. 2b and Fig. 2d) that is not present during cooling (Fig. 2c). This trend is consistent with the development of internal bias generated in poled samples where the polarization hysteresis loop shifts back to the origin when the temperature exceeds 320 K (Figure S7), suggesting that this relaxation peak is associated with the establishment of the internal field observed in the polarization hysteresis loop of poled samples. This additional relaxation peak (observed in Fig. 2b and Fig. 2d) no longer obeys either Debye-like relaxation or its derivative Havriliak-Negami model (see Figure S9 for more detail). Other models, such as Arrhenius type nearest-neighbor hopping, the variable-range hopping model (VRH)[28], or a model within the framework of a spin glass[29], cannot fit this curve either. Instead, the only reasonable model found is to combine both Debye-like and non-Debye-like relaxation as proposed by Mocedo et al.[30], originally to treat the relative roles of free and activation energy in the viscosity of liquids. The model considers that the relaxation acts as an occurrence of two simultaneous events: the "molecule" must attain sufficient energy to break away from its neighbors and change its orientation, and there also must be a site with a defect in the vicinity of the moving "molecule" with sufficient local free volume for a reorientation to occur[31-33]. Here we adapt this model to treat the reorientation of the oxygen vacancy to transform the defect as analogous to the defect formation in the model of Mocedo et al. et al.[30] with the corresponding reordering of the lattice distortion taking the role of molecular reorientation. There is no possibility for the transition associated with the permittivity peaks to be related to average structure change in the centrosymmetric rutile TiO_2. A careful XRD experimental and subsequent structural refinement as well as SHG measurement on both fresh and poled samples excluded the symmetry lowering of average structure. The DFT calculation also indicates that the centrosymmetric

structure of TiO_2 retains a similar crystal lattice after Mg doping, and there are no major structural instabilities. Thus, it is the short-range structure of the defects that appear to play the pivotal role. Based on these insights and the results of the DFT calculations described below, we suggested a relation where both reorientation of defect-dipoles and associated simultaneous defect transitions are considered (see Supplementary Information Section II for details)[31-33]:

$$f = f_0 \exp[\frac{E_a}{k_B(T-T_0)} + C\exp(-\frac{E_d}{k_B T})]^{-1} \quad (1)$$

f_0 is the "eigen frequency" of dipoles (the frequency beyond which the dipole cannot respond to the changing field); C is a constant and is related to the concentration of defects; E_a and E_d are the activation energy of the lattice response and "defect formation" energy (i.e. the energy required to form an Mg''_{Ti}-$V_O^{\bullet\bullet}$ defect pair), respectively; and T_0 is the critical temperature of the transition. It is found that Equation (1) fits the experimental data very well (see Fig. 2e), giving reasonable parameters within the framework of ionic polarization[28] as follows: f_0 =1.91×10^{12} Hz, E_a =0.0438 eV, E_d =1.6 eV, T_0 ~321.47 K. The defect formation energy is rather high but is quite consistent with our theoretical calculation results detailed later.

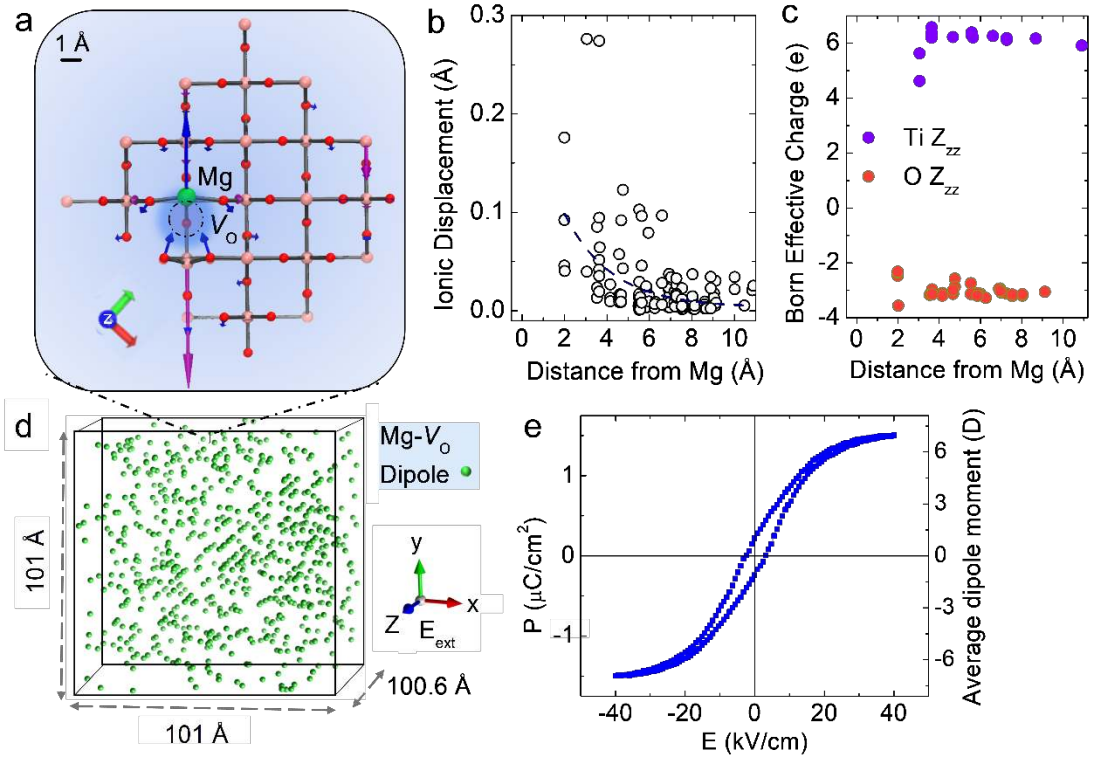

Fig. 3 Theoretical calculation of local defect states. **a** The local structure around the Mg''_{Ti}-$V_O^{\bullet\bullet}$ complex modelled with density functional theory shows significant ionic relaxation, with both oxygen and titanium displacements relative to pure rutile TiO_2. The blue arrows reflect the displacement within the crystal structure. **b** Ionic displacements relative to pure rutile as a function of radial distance from the Mg defect, indicating the majority of the ion displacement occurs in the vicinity of Mg-Vo defect pairs, within ~8Å scope from Mg ion. **c** Born-effective charges as a function of radial distance from the Mg defect. **d** Real-space image of the defect positions in the rutile supercell used in the Monte Carlo simulation. Titanium and oxygen are removed in the image for clarity. **e** Average dipole moment versus field in the simulation.

To clarify the physical mechanism behind the nonlinear dielectric behavior, we used a multi-scale theoretical approach based on density functional theory (DFT) and ensemble Monte Carlo (MC) finite-temperature simulations. DFT calculations were performed to understand the local structure on the scale of several Angstrom surrounding the Mg-V_O defect. Using the PAW DFT approach implemented in the Vienna Ab initio simulation package (VASP) software, ionic relaxation was performed for trial structures incorporating Mg into the rutile lattice. As might expected, titanium and oxygen displaced around the point defect. The lowest energy state was identified as the local structure illustrated in Fig. 3a. The magnitude of the ionic displacements relative to undoped rutile TiO_2 were found to correlate with the distance from the Mg''_{Ti}-$V_O^{\bullet\bullet}$ cluster, with the largest exceeding 0.25 Å (Fig. 3b).

To estimate the resulting polarization caused by the ionic displacements, density-functional perturbation theory was used[34] to calculate Born effective charges for ions in the Mg-doped structure. With the exception of the nearest-neighbors to the Mg''_{Ti}-$V_O^{\bullet\bullet}$ complex, the Born effective charges were found to be approximately constant for the Ti and O at 6 e and -3 e respectively as shown in Fig. 3c. The Born effective charge for Ti is strongly enhanced compared to its valence (4+), which is a typical feature for ferroelectric systems containing titanium, leading to so-called incipient ferroelectric behavior[35, 36]. To estimate the net change in polarization caused by the Mg defect, the Born charge tensors for each ion was multiplied by the displacement vector determined from the ionic relaxation relative to the unperturbed structure and summed over all atoms in the simulation to give the net polarization. The resulting polarization magnitude was calculated as 1.58 e.Å in the super cell containing one Mg. When multiplied by the 0.5 at% experimental concentration of Mg, this would produce a net polarization of 0.76 μC/cm^2 for an ensemble of

fully aligned dipoles. The calculated polarization is therefore in reasonable agreement with the experimental polarization (Fig. 1a), although additional effects play a role under real-world experimental conditions, namely the intrinsic linear response induced by the Ti atoms which increases the polarization systematically at higher fields, and the thermal fluctuations which reduce the dipole contribution at low fields.

The DFT calculations suggest that a defect dipole is nucleated by the presence of the Mg and its neighboring oxygen vacancy which then drives surrounding Ti^{4+} to move-off-center with large displacements, resulting in a "super" dipole. This, in turn, drives a relatively large spontaneous polarization compared with the normal intrinsic displacement of Ti^{4+} in rutile TiO_2. It is important to note that the majority of the polarization is induced by displacements within 8 Å scope of the Mg''_{Ti}-$V_O^{\bullet\bullet}$ complex (estimated from Mg ion), and displacements beyond this threshold barely affect the value of the calculated polarization. Thus, one can picture a region about one nanometer in diameter that operates as a dipole with a moment between 6.5 and 7.5 Debye. This dipole is very large compared to classical dipole glasses where the dipole moment is typically between 1-2 Debye, for example $(KI)_{1-x}(NH_4I)_x$[37]. The "super" dipole moment in the Mg''_{Ti}-$V_O^{\bullet\bullet}$ complex is intuitively expected based on a simple formal charge model if one considers the large separation between the Mg and the vacancy which has a formal charge of (2+). The DFT calculations, however, reveal a more complex picture involving the collaboration with the Ti displacements that minimize the energy. The direction of the polarization vector in the polarized nanoregion is co-aligned with the vector connecting the Mg and where the vacant oxygen would be. This implies that, should the vacancy undergo a short-range hop, which amounts to an oxygen switching sites in the local Mg distorted octahedral, the orientation of the dipole moment will likewise reorientate in that direction, by approximately 90°. The barrier for oxygen motion in rutile is strongly anisotropic, yielding low activation barriers in certain directions (<0.6 eV), and high barriers in other directions. This feature prevents long range diffusion of oxygen at room temperature, but allows short-range hops on slow time-scales[38, 39]. To understand the effect of the resulting ensemble of rotatable dipole moments at finite temperatures, Monte Carlo simulations were conducted using the calculated dipole moments predicted in the DFT.

Nonlinear susceptibility is a general feature well-known in systems where rotatable dipoles interact. For a spatially disordered ensemble of dipoles, the randomness of the interaction results in the so-called dipole glass which produces weakly hysteresis polarization-electric field (P-E) curves and

thermally activated aging phenomena below the glass transition[40]. The glass transition in the dipole glass is linearly proportional to the size of the larger effective dipole moments, and consequently, the large dipole moments unveiled by the DFT method discussed in the previous section are expected to foster an enhanced transition temperature relative to previously known dipole glasses[40]. Furthermore, in a highly-polarizable host, such as TiO_2, the interactions between dipoles may be enhanced by soft phonons that renormalize the naked electrostatic interaction, mitigating the effect of electrostatic screening and yielding higher transition temperature[40]. Rutile is a well-known case in which soft phonons occur[41], and make the system vulnerable to a ferroelectric instability. To test whether modified dipole interactions could yield nonlinear polarization, a numerical software model was created to simulate an ensemble of interaction dipoles within the rutile lattice under the experimental conditions. This was based on a large-scale Monte Carlo simulation to trial dipole configurations which was performed with a simultaneous self-consistent electrostatic calculation that includes the effect of the dipole-dipole interaction for a spatially disordered array of 700 dipoles fixed in a lattice, where the internal field is solved self-consistent with the external applied field (More details see Methods).

Fig. 3d shows a real-space picture of the defect dipole spatial correlations on the rutile lattice used to simulate the 0.5 at% Mg concentration as an example of a microstructural configuration. Freezing phenomena are well known in canonical spin glasses, and dipole glasses. Fig. 3e shows the field-response of the dipole-induced polarization at 300 K in the simulation, indicating a nonlinear response in the quasi-static regime below the glass transition. The nonlinear response and magnitude of maximum polarization are relatively consistent with our experimental results. This suggests that a super dipole glass caused by the strong dipole-dipole interactions of the polarized nanoregions surrounding the Mg dopants is an excellent candidate to feasibly explain the mechanism behind the induced nonlinear susceptibility and the relaxation in the temperature dependent spectrum. A key finding is that the metastable states in the simulation produced long-lived polarization that relaxes gradually.

Given that the nonlinear polarization can be explained by the collective dipole glass state, we further calculated the probability of alignment/dealignment of Mg''_{Ti}-$V_O^{\bullet\bullet}$ that give the only possible reason for the poling induced abnormal phenomenon: poling-electric-field-dependent internal bias observed in polarization hysteresis loop of poled samples. The alignment/dealignment should be related to the motion of the local oxygen vacancy. Our calculations suggest that there

are two possible sites for oxygen vacancy to move. One is move around the 4 equatorial oxygen atom position, which needs to surmount an energy barrier of ~1.3 eV, while the move to axial position requires a much higher energy of ~1.8 eV. Both energies are quite high but is also close to the mean energy of 1.6 eV calculated from the temperature dielectric spectra.

These results further confirm that the model we use to fit the poling induced dielectric relaxation and the DFT calculations are consistent and reliable. The correlation between local polar-regions and the hopping of oxygen vacancies under an applied electric field is responsible for the origins of the abnormal polarization. It is also known that short-range phonon interactions in site-disordered glasses can potentially reverse the sign of the internal interactions[40], leading to a scenario that has close similarities with similar anomalies found in magnetic exchange bias systems when interfacial exchange constants are reversed[42]. This discovery is rather serendipitous, it tells us that not only can the Mg_{Ti}''-$V_O^{\bullet\bullet}$ defect dipoles polarize the surrounding Ti^{4+} to give rise to a collective super dipole glass behavior, but also demonstrates, for the first time, that the reorientation of such defect-dipoles behaves fundamentally differently from ionic displacement, due to a combination of lattice response and defect transformation.

We should here emphasize that the polarization hysteresis loop observed in such a doped TiO_2 seems analogous to ferroelectrics but obviously there are also underlying differences because the structure is centrosymmetric. It is also phenomenologically analogous to electrets (e.g. ferroelectrets) which are dielectric materials that have a quasi-permanent electric charge or dipole polarization by surface charges, space charge and oriented/aligned dipoles[43, 44]. However, we are not aware of any report of an electret in an inorganic oxide which exhibits an anomalous polarization mechanism like the one we have observed in Mg doped rutile TiO_2. The property presented in Mg-doped TiO_2 is non-ferrroelectric, non-linear polarisation behaviour. This also differs from the ferroelectricity reported in doped HfO_2 with hetero-valent ions such as Y, Al, and La and even homovalent ions such as Si and Zr[20-22] where the ferroelectricity in doped HfO_2 is claimed to be originated from defect-stabilized polar orthorhombic phase but still need further clarifying.[20-22] It also can be distinguished from (Nb,Al) co-doped TiO_2,.[23] where the ferroelectricity is determined only based on the observable polarisation hysteresis loop, attributed to Nb-Al pairs. To decrease potential misleading or controversy, we therefore use abnormal nonlinear polarization rather than ‘ferroelectric-like’ or ‘electret’ to distinguish the phenomena

from the effects observed in traditional ferroelectric and electret materials as well as defect-induced ferroelectricity.

This study provides compelling experimental and theoretical evidence that nonlinear electrical polarization in centrosymmetric rutile TiO_2 can be achieved by defect-driven symmetry breaking. The defect dipole introduced by the presence of sterically mismatched Mg^{2+} coupled with a neighboring oxygen vacancy significantly polarizes its surrounding Ti^{4+} to move-off-center, leading to an enhanced dipole moment that is large enough to engender giant permittivity. The interaction between these dipolar defects gives rise to abnormal nonlinear electrical polarization stable to high temperature, behaving similarly to but not being ferroelectricity. The Mg-doped rutile TiO_2 is just one example, similar non-linear polarization behavior was also found in Ni-doped rutile TiO_2 (Figure S10). Though the net polarization in the doped rutile TiO_2 is low compared to conventional ferroelectrics, it should be recognized that the defect dipoles caused by the Mg-doping are present in much smaller atomic concentrations than the tightly-packed dipoles in a ferroelectric. Consequently, the individual moment per dipole surrounding the Mg is actually very large, and the limiting factor is the concentration of the dipoles. Thus, with further development of the understanding of the mechanism, it is highly possible that this feature can be exploited to produce higher polarizations, e.g. by using other forms of TiO_2 or other materials to increase the doping level.

In summary, we here broke traditional approach by introducing a new strategy for defect engineering, in which a trace of 'difficult-to-dope 'ions are introduced into a host material. Such 'difficult-to-dope' ions are defined as local chemically, extremely unhappy ions in host materials. They cannot stand alone as an individual substitutional ion and must couple with a surrounding chemical environment change, leading to a "butterfly effect"- to significantly change the property of materials even create new function that traditionally should be impossible to appear in host materials. The centrosymmetric rutile TiO_2 with less than 1 at% doping level of Mg^{2+} ions (difficult-to-dope ions), as an example, presents a large nonlinear polarization behavior like a typical ferroelectricity, but it is not ferroelectric material as defined traditionally. We believe these results would significantly advance the understanding of defect chemistry and condensed matter physics.

Methods

Experimental section. Nonstoichiometric rutile TiO_2-based ceramic samples were prepared by conventional solid-state reaction method. $Mg_xTi_{1-x}O_{2-\delta}$ (with a nominal composition of x=0.25 at%, 0.5 at%, 1 at% and 5 at%) and $Ni_yTi_{1-y}O_{2-\delta}$ (with a nominal composition y=0.5 at%) were synthesized by a conventional solid-state reaction method where rutile TiO_2 (99.99%, Aldrich), MgO (99.99%, Aldrich), and NiO (99.99%, Aldrich) were used as raw materials. Doped rutile TiO_2 and pure rutile TiO_2 ceramics with relative density ~96-98% were successfully prepared under optimized conditions at 1300~1400 ^oC for 2 to 4 hours. All ceramic pellets were well polished and then coated with silver on both sides, then heat treated at 550 ^oC for 30 min to ensure good electrical contact. Sputtered-gold Au electrodes were also coated onto the ceramic pellets for comparison purposes. The structure of the resultant samples was then studied using X-ray powder diffraction (XRD) (PANalytical Empyrean). The XRPD patterns were collected under the following conditions: 45 kV, 40 mA, 1.54Å (Cu Kα), scanning rate-0.3^o/min, scanning step-0.02 ^{o}, Panalytical pixel1D detector and Highscore Plus software were used to collect and process the data for further analysis. The Electron paramagnetic resonance (EPR) Continuous wave X-band EPR measurements were performed at the working frequency of 9.38 GHz and by using a Bruker E500 spectrometer, equipped with an Oxford Instruments EPR 935 cryostat and ITC4 temperature controller. The modulation amplitude was set between 0.2 to 2 mT. Bruker-Xepr 2.6b.167 software was used to collect EPR signals of our samples. Prior to the EPR measurement of Mg doped TiO_2, we firstly collected the EPR signal of one blank quartz tube at the temperature of about 10 K in order to exclude possible effects of sample holders, and then used it as a background or reference. Field emission scanning electron microscopy (SEM, Zeiss Ultraplus) in conjunction with an energy dispersive X-ray spectrometer (INCA Energy 450 EDXA system), back scattered electron image (BSE) and secondary electron image (SE) were used to confirm the homogeneous phase of the acceptor ion doped rutile TiO_2. For the SEM measurement, the ceramic samples were first polished with different grade of silicon carbide abrasive papers from Grit 600 to Grit4000, following with different grade of diamond paste from 10 µm to 0.25 µm, and finally cleaned by repetition of ultrasonic bath with ethanol and dried. The second harmonic generation (SHG) experiment was performed with a fundamental wave generated from a pulsed Nd-YAG laser (Spectra-Physics, GRC-150-30, maximum pulse energy of 200mJ) with tunable energy at a repetition rate of 30 Hz and wavelength of 1064nm in a reflection mode. The measurements of polarization-electric field (P-E) loops and current-electric field (I-E) were carried out using an

AixACCT ferroelectric test unit in conjunction with a laser interferometer. The sample was immersed in silicone oil to prevent arcing during the measurement.

DFT calculation. Calculations were performed under periodic boundary conditions using the PAW DFT approach implemented in the Vienna Ab initio simulation package (VASP) software using the PBE functional. 12, 6 and 10 electrons were treated as valance for Ti, O and Mg, respectively. Ionic relaxation was performed, allowing titanium and oxygen to displace around the point defect. To model the effect of low Mg doping concentration, 2×2×3 and 3×3×4 supercells based on unperturbed rutile TiO_2 were constructed. Mg was then substituted to replace a single titanium atom. An oxygen atom was removed for charge balance. The total energy depended strongly on the location of the oxygen vacancy, with vacancies adjacent to the substituted Mg being the most stable. Ionic displacements were calculated relative to the unperturbed reference positions in pure rutile TiO_2. The size and direction of the displacements were compared in the 3×3×4 and 3×2×2 cell where possible and found to be nearly identical indicating that the effect of self-interaction of the Mg defects through the periodic boundary conditions is minimal.

To estimate the resulting polarization caused by the ionic displacements, density-functional perturbation theory was used[34] to calculate the Born effective charges (Z_{ij}^{n}). These relate the polarization and the ionic displacements according to the well-known Equation (2):

$$Z_{ij}^{n} = \frac{\Omega}{e}\frac{\partial P_i^n}{\partial u_j^n} \quad (2)$$

where n is the numeric label unique to each Ti, Mg and O in the simulation, Ω is the unit cell volume, e is the fundamental charge on an electron, P_i^n is the polarization component in the Cartesian direction i, and u_j^n is the displacement of the ion in the Cartesian direction j.

To estimate the net change in polarization caused by the Mg defect, the Born charge tensors for each ion was multiplied by the displacement vector determined in the ionic relaxation and summed over all n atoms in the simulation to give the net polarization in along the direction i:.

$$P_i = \sum_{n}^{n=N} Z_{ij}^{n}\, \partial u_j^n - P(0) \quad (3)$$

The reference state $P(0)$ was taken against the undistorted structure of rutile TiO_2.

Monte Carlo Simulations. The simulation model was established based on the Monte Carlo simulation to trial dipole configurations. This was performed with a simultaneous self-consistent

electrostatic calculation that includes the effect of the dipole-dipole interaction for a spatially disordered array of dipoles fixed in a lattice. This method is very similar to previous simulations of freezing phenomena in dipole glasses.[45, 46] In the model, the microscopic dipole undergoes reorientation to minimize their energies in the internal field according to a standard heat bath algorithm.[47] The dipole directions are restricted to point along one of 6 Cartesian directions reflecting the limited number of oxygen vacancy positions available in the local Mg octahedral—a "clock" model. The dipole defects were randomly substituted onto the titanium sites with a probability of 0.5% corresponding to the experimental atomic Mg concentration. A total of 580 interaction defect dipoles were included in the simulation. At each measurement point, the simulation was equilibrated for 1000 Monte Carlo steps to allow the internal dipole configurations to reach a self-consistent solution. As the microstructural configuration of the dipole depends on the random seed, the results were averaged over five separate microstructural configurations in order to show that they were statistically robust.

The energy of the dipole system has four main components

$$\mathrm{H} = H_{d-d} + H_{ext} + H_L + H_D \quad (4)$$

The first term $H_{d\text{-}d}$ is the local field caused by the dipole-dipole interaction energy describing the electrostatic force which can act to align or de-align dipoles depending on their relative separation in space, and their dipole direction. The second term H_{ext} is the effect of the external field, from the electrode on the sample, which tends to align dipoles in the direction of the applied field. The third term H_L is the Lorentz-field which accounts for the long-range effects of polarization on the electrostatic boundary condition in a continuum approximation. The final term H_D is the depolarizing field, which accounts for the fields from surface charges or induced charges, which depending on the sample's shape may tend to set up a field that is counter to the external field, thereby acting to reduce the internal polarisation of the dipoles. Energetically, the most important component of the model is the dipole-dipole interaction, which is calculated self-consistently using the electric field from the entire ensemble of dipoles as they evolve in the simulation:

$$\boldsymbol{E_i}(\mathbf{r}) = \frac{1}{4\pi\varepsilon}\left[\frac{3(\boldsymbol{p_i}\cdot\boldsymbol{r})\boldsymbol{r}}{r^5} - \frac{\boldsymbol{p_i}}{r^3}\right] \quad (5)$$

$$\boldsymbol{E_D^T}(\boldsymbol{r_j}) = \sum_{i,i\neq j}^{j} \boldsymbol{E_i}(\mathbf{r}) \quad (6)$$

A cut-off 40 Å was used in evaluating the real-space dipole summation. The potential energy of the dipole interacting with the surrounding field is then

$$H_{d-d} = \boldsymbol{p_j} \cdot \boldsymbol{E_D^T}(\boldsymbol{r_j}) \quad (7)$$

The other terms have a simple form analogous to Equation (7) using simple scalar fields, and for the purposes of discussing these preliminary results have thus been absorbed into an effective non-local electric field H_{eff} for computational simplicity. H_{eff} thus includes all of the long-range field interactions, which are primarily determined by the applied electric field from the electrodes, but also the smaller effects of depolarization and the reaction field (equivalent to the Ewald summation) driven by the global dielectric behavior.

Code availability. The Monte Carlo simulation codes used in this study can be made available from the corresponding authors upon request.

Data availability. The experimental and modeling data that support the findings of this study are available from the corresponding authors upon request.

Acknowledgements

WD, TL, DC, TJF and YL acknowledge the support of the Australian Research Council (ARC) in the form of Discovery Projects (DP1601104780). The authors acknowledge the facilities and the scientific and technical assistance of the Australian microscopy and microanalysis research facility (AMMRF) at the Centre of advanced Microscopy, the Australian National University. This work is supported by the International Science and Technology Cooperation Program of China (Grant Nos. 2015D FA51100).

Author contribution

WD conducted the sample synthesis, characterization of chemistry, structure and property with assistance of TL, QS, WH and HC. DC and TF as well as LJ conducted the multi-scale theoretical approach based on density functional theory (DFT) and ensemble Monte Carlo (MC) finite-temperature simulations. TL and QL conducted a careful structural analysis and synchrotron characterization. NN, DY, AC and XW were heavily involved in discussion with regards to the mechanism. GW and MGH conducted the SHG studies. YL initiates the project, supervise experimental work and coordinate theoretical research with DC and TF. WD, DC, TF and YL draft the manuscript. All the authors revised and polished the manuscript.

Additional information

Supplementary information is available in the online version of the paper. Reprints and permissions information is available online at xxxx.

Completing financial interests

The authors declaim no competing financial interests.

References

1. X. Ren, *Nat. Mater.*, 2004, **3**, 91-94.
2. I. Grinberg, D. V. West, M. Torres, G. Gou, D. M. Stein, L. Wu, G. Chen, E. M. Gallo, A. R. Akbashev, P. K. Davies, J. E. Spanier and A. M. Rappe, *Nature*, 2013, **503**, 509-512.
3. W. Hu, Y. Liu, R. L. Withers, T. J. Frankcombe, L. Norén, A. Snashall, M. Kitchin, P. Smith, B. Gong, H. Chen, J. Schiemer, F. Brink and J. Wong-Leung, *Nat. Mater.*, 2013, **12**, 821-826.
4. A. Walsh and A. Zunger, *Nat. Mater.*, 2017, **16**, 964-967.
5. Q. Sun, C. Zheng, L. Q. Huston, T. J. Frankcombe, H. Chen, C. Zhou, Z. Fu, R. L. Withers, L. Norén, J. E. Bradby, J. Etheridge and Y. Liu, *J. Phys. Chem. Lett.*, 2017, **8**, 3249-3255.
6. Q. Sun, D. Cortie, S. Zhang, T. J. Frankcombe, G. She, J. Gao, L. R. Sheppard, W. Hu, H. Chen, S. Zhuo, D. Chen, R. L. Withers, G. McIntyre, D. Yu, W. Shi and Y. Liu, *Adv. Mater.*, 2017, **29**, 1605123-n/a.
7. Z. Gai, Z. Cheng, X. Wang, L. Zhao, N. Yin, R. Abah, M. Zhao, F. Hong, Z. Yu and S. Dou, *J. Mater. Chem. C*, 2014, **2**, 6790-6795.
8. X. J. Cheng, Z. Li and J. Wu, *J. Mater. Chem. A*, 2015, **3**, 5805-5810.
9. W. Dong, W. Hu, A. Berlie, K. Lau, H. Chen, R. L. Withers and Y. Liu, *ACS Appl. Mater. Interfaces*, 2015, **7**, 25321-25325.
10. W. Dong, W. Hu, T. J. Frankcombe, D. Chen, C. Zhou, Z. Fu, L. Cândido, G. Hai, H. Chen, Y. Li, R. L. Withers and Y. Liu, *J. Mater. Chem. A*, 2017, **5**, 5436-5441.
11. W. Dong, D. Chen, W. Hu, T. J. Frankcombe, H. Chen, C. Zhou, Z. Fu, X. Wei, Z. Xu, Z. Liu, Y. Li and Y. Liu, *Sci. Rep.*, 2017, **7**, 9950-9957.
12. A. Tkach, O. Okhay, A. Almeida and P. M. Vilarinho, *Acta Mater.*, 2017, **130**, 249-260.
13. D. Huang, Z. Liu, Y. Li and Y. Liu, *J. Alloy Compd.*, 2017, **698**, 200-206.
14. Y. Song, X. Wang, X. Zhang, X. Qi, Z. Liu, L. Zhang, Y. Zhang, Y. Wang, Y. Sui and B. Song, *Appl. Phys. Lett.*, 2016, **109**, 142903.
15. Z. Wang, M. Cao, Q. Zhang, H. Hao, Z. Yao, Z. Wang, Z. Song, Y. Zhang, W. Hu and H. Liu, *J. Am. Ceram. Soc.*, 2015, **98**, 476-482.
16. K. Pyka, J. Keller, H. L. Partner, R. Nigmatullin, T. Burgermeister, D. M. Meier, K. Kuhlmann, A. Retzker, M. B. Plenio, W. H. Zurek, A. del Campo and T. E. Mehlstäubler, *Nat. Commun.*, 2013, **4**, 2291.
17. G. Sala, M. J. Gutmann, D. Prabhakaran, D. Pomaranski, C. Mitchelitis, J. B. Kycia, D. G. Porter, C. Castelnovo and J. P. Goff, *Nat. Mater.*, 2014, **13**, 488-493.
18. M. Winter.
19. *The bond valence approach at http://kristall.uni-mki.gwdg.de/softbv/ (Date of acess: 09/10/2016).*

20. T. S. Böscke, J. Müller, D. Bräuhaus, U. Schröder and U. Böttger, *Appl.Phys. Lett.*, 2011, **99**, 102903.
21. J. Müller, T. S. Böscke, U. Schröder, S. Mueller, D. Bräuhaus, U. Böttger, L. Frey and T. Mikolajick, *Nano Lett.*, 2012, **12**, 4318-4323.
22. T. Shimizu, K. Katayama, T. Kiguchi, A. Akama, T. J. Konno and H. Funakubo, *Appl. Phys. Lett.*, 2015, **107**, 032910.
23. Y. Yu, L.-D. Wang, W.-L. Li, Y.-L. Qiao, Y. Zhao, Y. Feng, T.-D. Zhang, R.-X. Song and W.-D. Fei, *Acta Mater.*, 2018, **150**, 173-181.
24. S. K. B. Srivastava, M.; Brahma, B.; Bouzerar, G., *Cond. Matter Mater. Sci.*, 2015, **arXiv preprint arXiv:1510.04782**.
25. J. Wang, M. Qin, H. Tao, W. Ke, Z. Chen, J. Wan, P. Qin, L. Xiong, H. Lei, H. Yu and G. Fang, *Appl. Phys. Lett.*, 2015, **106**, 121104.
26. W. H. Meiklejohn and C. P. Bean, *Phys. Rev.*, 1957, **105**, 904-913.
27. S. Havriliak and S. Negami, *Polymer*, 1967, **8**, 161-210.
28. A. K. Jonscher, *Chelsea Dielectrics Press.*, 1996.
29. J. A. Mydosh, *Spin Glasses: An Experimental Introduction*, Taylor & Francis, 1993.
30. P. B. Macedo and T. A. Litovitz, *J. Chem. Phys.*, 1965, **42**, 245-256.
31. Y. Ryabov, A. Gutina, V. Arkhipov and Y. Feldman, *J. Phys. Chem. B*, 2001, **105**, 1845-1850.
32. A. Gutina, T. Antropova, E. Rysiakiewicz-Pasek, K. Virnik and Y. Feldman, *Microporous Mesoporous Mater.*, 2003, **58**, 237-254.
33. L. Tong, J. Sun, S. Wang, Y. Guo, Q. Li, H. Wang and C. Wang, *RSC Adv.*, 2017, **7**, 50680-50687.
34. G. Kresse, M. Marsman and J. Furthmuler, *https://cms.mpi.univie.ac.at/vasp/vasp/LEPSILON_static_dielectric_matrix_ion_clamped_piezoelectric_tensor_Born_effective_charges.html#incar-epsilon (Date of acess: 09/09/2016)*.
35. M. E. Lines, Glass, A. M., *Clarendon Press, Oxford, 1977*, 1977.
36. S. E. Rowley, L. J. Spalek, R. P. Smith, M. P. M. Dean, M. Itoh, J. F. Scott, G. G. Lonzarich and S. S. Saxena, *Nat. Phys.*, 2014, **10**, 367-372.
37. I. Fehst, R. Böhmer, W. Ott, A. Loidl, S. Haussühl and C. Bostoen, *Phys. Rev. Lett.*, 1990, **64**, 3139-3142.
38. Z. Zhang, Q. Ge, S.-C. Li, B. D. Kay, J. M. White and Z. Dohnálek, *Phys. Rev. Lett.*, 2007, **99**, 126105.
39. H. Iddir, S. Öğüt, P. Zapol and N. D. Browning, *Phys. Rev. B*, 2007, **75**, 073203.
40. B. E. Vugmeister and M. D. Glinchuk, *Rev. Mod. Phys.*, 1990, **62**, 993-1026.
41. B. Wehinger, A. Bosak and P. T. Jochym, *Phys. Rev. B*, 2016, **93**, 014303.
42. J. Nogués, D. Lederman, T. J. Moran and I. K. Schuller, *Phys. Rev. Lett.*, 1996, **76**, 4624-4627.
43. M. É. Borisova and S. N. Koikov, *Sov. Phys. J.*, 1979, **22**, 58-69.
44. R. Gerhard-Multhaupt, *Wiley Encyclopedia of Electrical and Electronics Engineering*, 1999, DOI: doi:10.1002/047134608X.W2825.
45. T. Y. Yoshiaki Tanida, Hiroumi Ishii, *J. Phys. Soc. JPN*, 1988, **57**, 2168-2173.
46. R. Medina, R. Nava and M. Saint-Paul, *Solid State Commun.*, 1984, **50**, 51-53.
47. D. Cortie and J. Pillans, *J. Comput. Sci.*, 2011, **2**, 279-285.

Supplementary Information

Collective nonlinear electric polarization via defect-driven local symmetry breaking

Wen Dong[1,2], David Cortie[1,3,4,*], Teng Lu[1], Qingbo Sun[1], Narendirakumar Narayanan[1,3], Wanbiao Hu[1], Lilit Jacob[5], Qian Li[6], Dehong Yu[3], Hua Chen[7], Aiping Chen[8], Xiaoyong Wei[9], Genmiao Wang[1], Mark G. Humphrey[1], Terry J. Frankcombe[5,*] and Yun Liu[1,*]

[1] Research School of Chemistry, The Australian National University, ACT 2601, Australia.

[2] Department of Physics, University of Warwick, Gibbet Hill Road, Coventry CV4 7AL, UK

[3] Australia Nuclear Science and Technology Organisation, Lucas Height, NSW 2234, Australia.

[4] Institute for Superconducting and Electronic Materials, University of Wollongong, Innovation Campus, Squires Way, North Wollongong, NSW 2500, Australia.

[5] School of Physical, Environmental and Mathematical Sciences, The University of New South Wales, Canberra, ACT 2601, Australia.

[6] Advanced Photon Source Facility, Argonne National Laboratory, Lemont, IL 60439, USA.

[7] Centre for Advanced Microscopy, The Australian National University, ACT 2601, Australia

[8] Center for Integrated Nanotechnologies (CINT), Los Alamos National Laboratory, Los Alamos, NM 87545, USA.

[9] Electronic Materials Research Laboratory, Key Laboratory of the Ministry of Education & International Center for Dielectric Research, Xi'an Jiaotong University, Xi'an, 710049, China

*To whom the correspondence should be addressed: dcortie@uow.edu.au, t.frankcombe@adfa.edu.au and yun.liu@anu.edu.au

I. Characterizations

Structure and phase characterizations

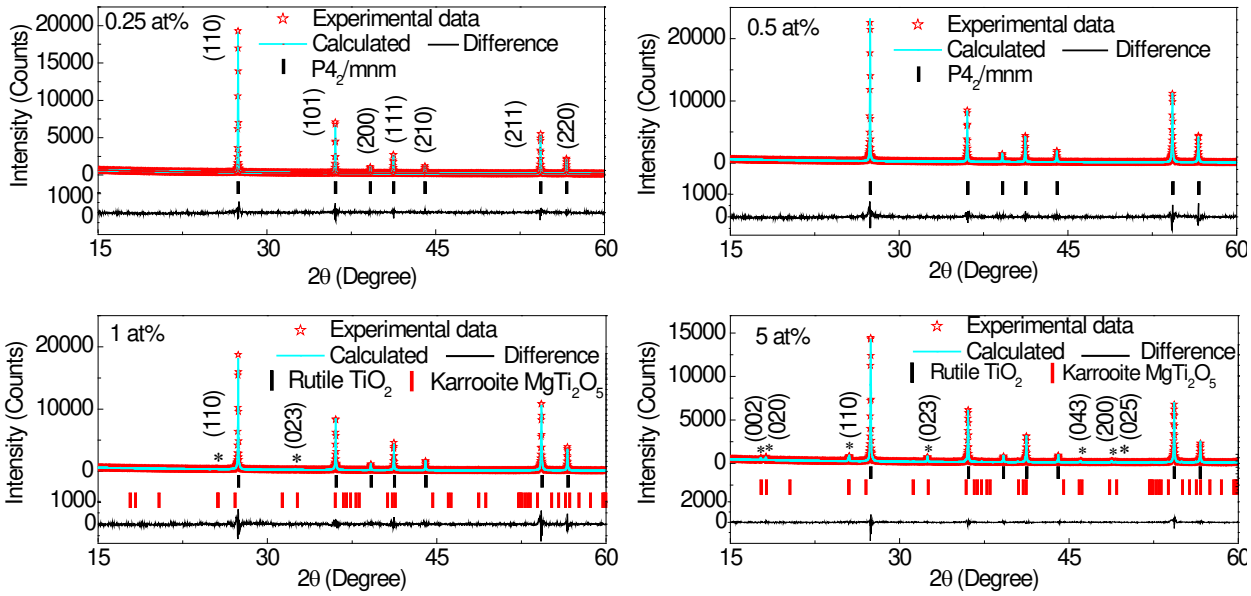

Figure S1. Structure and phase characterization of $Mg_xTi_{1-x}O_{2-\delta}$ at different doping levels (a x=0.25 at%, b x=0.5 at%, c x=1 at%, and d x=5 at%). The black and red bars at the bottom of each graph are the standard diffraction patterns for rutile TiO_2 pattern (JCPDS No. 21-1276) and orthorhombic $MgTi_2O_5$ pattern (JCPDS No. 98-003-7232), respectively. All the figure shows the experimental XRD data and the calculated pattern by Jana2006, the negligible variation in the difference confirm the good calculation. For the sample presenting the single rutile phase, the unit-cell parameters exhibit a small expansion with increasing the Mg content (a=4.5949(5) Å, c=2.9597(4) Å for x=0.25 at% and a=4.5963(5) Å, c=2.9606(5) Å for 0.5 at%), which is possibly due to the larger ionic radius of Mg^{2+} in comparison with Ti^{4+}. Moreover, as the doping level increases, the relative intensity of some diffraction peaks change obviously. For example, the peak intensity $I_{(211)}$ at (211) and its ratio (i.e. $I_{(211)}/I_{(110)}$=0.285 for x=0.25 at%, and $I_{(211)}/I_{(110)}$=0.474 for x=0.5 at%,) relative to the main peak increase obviously, suggesting the change of the atomic position or the preferred orientation after the introduction of Mg with larger ionic radius into the host rutile TiO_2 structure, which has been similarly observed in rutile TiO_2 doped with sterically mismatched In^{3+} ions. While, for sample with higher doping levels (1 at% to 5 at%), the pattern needs to be fitted by rutile TiO_2 phase and orthorhombic $MgTi_2O_5$ phase. Two characteristic peaks of the orthorhombic $MgTi_2O_5$ in the x=1 at% sample, including (110) and (023) indicated by asterisks, can be observable. And more characteristic peaks are significant in the 5 at% as shown in Figure S1d with asterisks and indexed as well. These XRD analyses suggest the doping limits of Mg into the rutile TiO2 is less than 1 at%, which is in a good agreement with the results reported previously[1, 2].

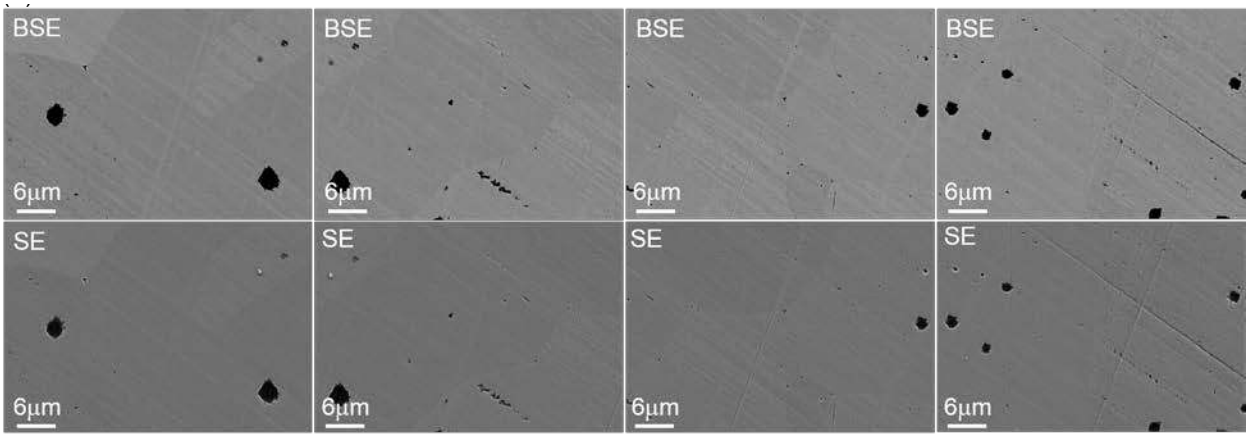

Figure S2. Four BSE images (up, from left to right) and corresponding SE images (down, from left to right) scanned in an area on surface of 0.5 at at% Mg-doped rutile TiO_2 where the areas were chosen so that each of the right-hand images partially overlaps with the image to the left, to depict a continuous scanning area.

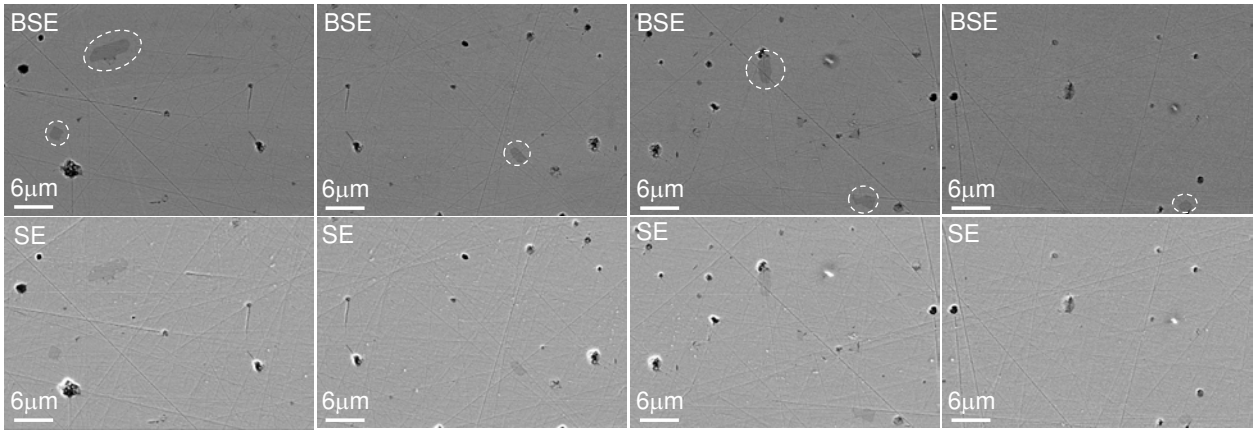

Figure S3. Four BSE images (up, from left to right) and corresponding SE images (down, from left to right) scanned in an area on surface of 1 at% Mg-doped rutile TiO_2 where the areas were chosen so that each of the right-hand images partially overlaps with the image to the left, to depict a continuous scanning area.

Mg-doped rutile TiO_2 shows a pure rutile phase at low doping levels. The XRD patterns of the synthesized samples indicates that the Mg-doped rutile TiO_2 contains a second phase of $MgTiO_3$, as shown by the peaks within the blue rectangular regions at doping level beyond 1 at% (Figure S1). The main reason for this is that the ionic size of Mg^{2+} (86 pm) is much larger than that of the Ti^{4+} (74.5 pm). According to the bond valence sum (BVS) calculation,[3] replacing the Ti^{4+} with Mg^{2+} in the rutile TiO_2 average structure gives a 30.6% over-bonded, apparent valence (AV) for the Mg^{2+} ion of +2.6121, which makes the structure instability index to be about 0.3119. The high

structure instability makes it hard for high concentration of Mg to be soluble in rutile TiO_2, thus resulting in secondary phase. Our results are also consistent with the reported literature that small amount of Mg can be doped into TiO_2.[1, 2] To further confirm the Mg was doped into the rutile TiO_2, the pure phase of the Mg doped rutile TiO_2 at relatively low levels, e.g. 0.5 at%, microstructure, element distribution and chemical composition were determined by field emission scanning electron microscopy (SEM, Zeiss Ultraplus) in conjunction with an energy dispersive X-ray spectrometer (INCA Energy 450 EDXA system), back scattered electron image (BSE) and secondary electron image (SE) were used to confirm the pure phase of the 0.5 at% Mg-doped rutile TiO_2, particularly, we randomly scanned four continued areas on 0.5 at% (Figure S2) and 1 at% (Figure S3) Mg-doped rutile TiO_2 for comparison. To prove the images from left to right are continuous, the images on the left partially overlap with the adjacent ones on the right. It is obvious from Figure 1b that there is no secondary phase within the grain or grain-boundary in 0.5 at% Mg doped rutile TiO_2, indicating a homogenous chemical composition distribution, while, in contrast, the 1 at% Mg doped rutile TiO_2 typically shows obvious secondary phase in each image as shown in Figure S3. Therefore, there is no secondary phase observable in the images in 0.5 at% Mg doped rutile TiO_2 while there is obvious secondary phase in the 1 at% Mg doped rutile TiO_2. These results are consistent with the XRD pattern that the 0.5 at% Mg doped rutile TiO_2 shows a pure rutile TiO_2 phase. In light of these considerations, we mainly focus on 0.25 at% and 0.5 at% Mg doped rutile TiO_2.

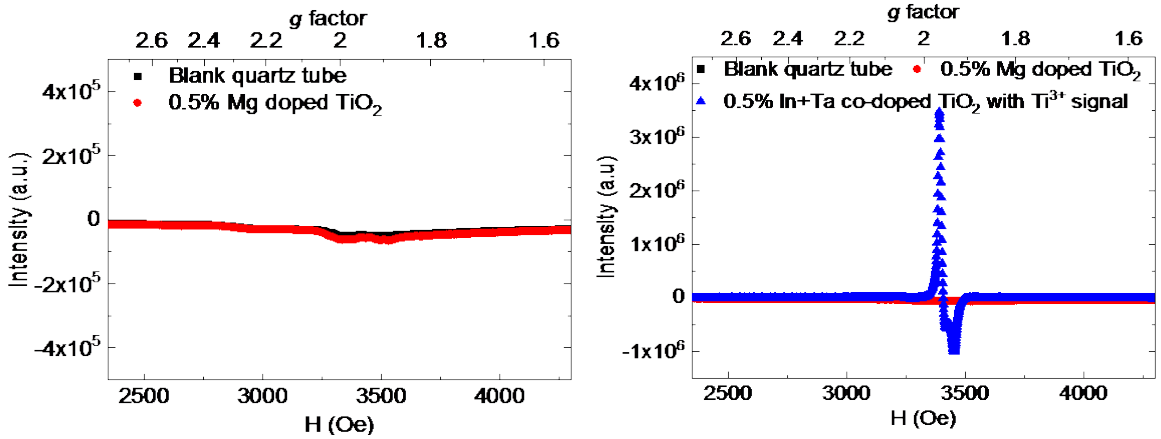

Figure S4 (a) EPR spectra of the blank quartz tube (black curve) as background and 0.5 at% Mg doped rutile TiO_2(red curve). (b) EPR spectrum of background (black curve), 0.5 at% Mg doped rutile TiO_2(red curve), and 0.5 at% In+Ta co-doped rutile TiO_2 (blue curve) with nominal composition $[(In_{0.5}Ta_{0.5})_{0.005}Ti_{0.995}O_2]$[4] where the signal of Ti^{3+} has been confirmed. Note: To make the comparison consistent, the weight of all the samples keeps ~0.1g and other

measurement conditions are also similar. As shown in Figure S4a, the quartz tubes did not have any EPR signal, demonstrating that they were well cleaned. When Mg doped TiO_2 with a doping level of 0.5 at% were added into the quartz tubes and also measured by the EPR instrument at 10 K, it almost presents the same EPR curve as that of quartz tube. Further comparing the EPR results of Mg doped TiO_2 with that of our other samples like In+Ta co-doped TiO_2 with nominal composition $[(In_{0.5}Ta_{0.5})_{0.005}Ti_{0.995}O_2]$ (Figure S4b) confirmed,[4] there is no obvious Ti^{3+} signal in the Mg doped TiO_2. In addition, we also did not find the EPR peak of $V_O^{\bullet}$ (i.e., one electron is trapped on oxygen vacancy) at around g=2.004 as generally reported.[5-7] Therefore, we claim that there were no Ti^{3+} and $V_O^{\bullet}$ in Mg doped TiO_2.

Electric polarization characterization

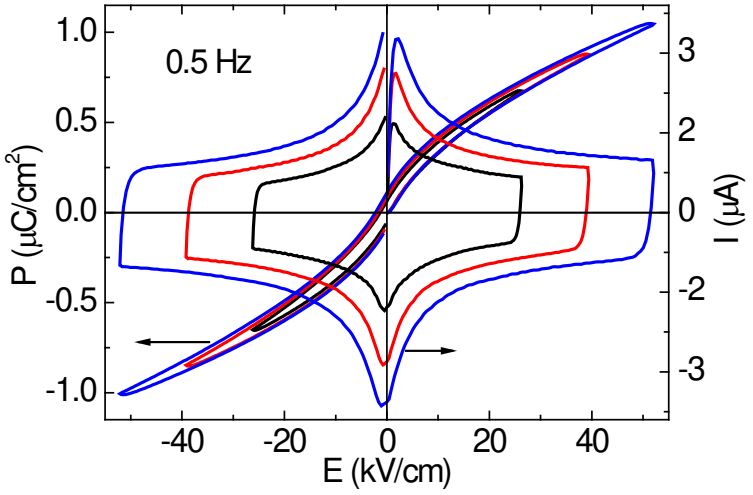

Figure S5 Voltage dependent P-E and I-E loops of fresh 0.25 at% Mg doped rutile TiO_2 measured at 0.5 Hz (first loop without pre-poling). The maximum polarization value and current increase with the increasing electric field measured at 0.5 Hz, where two current peaks are nearly symmetrical about x axis.

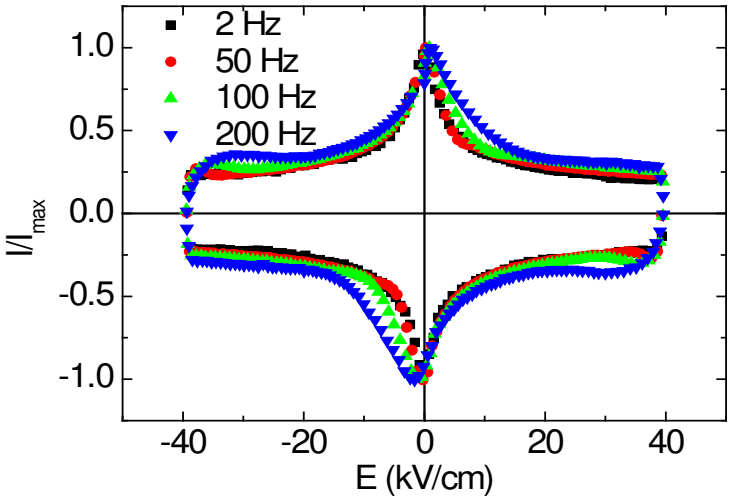

Figure S6 I-E loops of fresh 0.25 at% Mg doped rutile TiO_2 measured with a triangle electric field at the frequency of 2 Hz, 50 Hz, 100 Hz, and 200 Hz. The current is presented using a normalized current (for comparison). For the I-E loops measured at different frequencies, their overall shapes are quite similar except the shift of the current peaks, suggesting that the increase of the switching field with the increase of frequency, not as the same as behavior observed in a normal ferroelectricity.

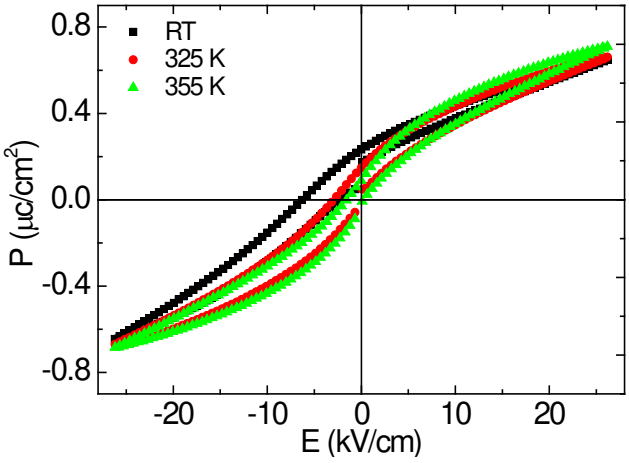

Figure S7 Temperature-dependent P-E loops selected at three temperature points at RT (black square), 325 K (red round), and 355 K (gree triangle) after the sample was negatively poled at room temperature. Increasing the temperature can reduce the internal bias and return to the fresh state once the temperature is sufficiently high.

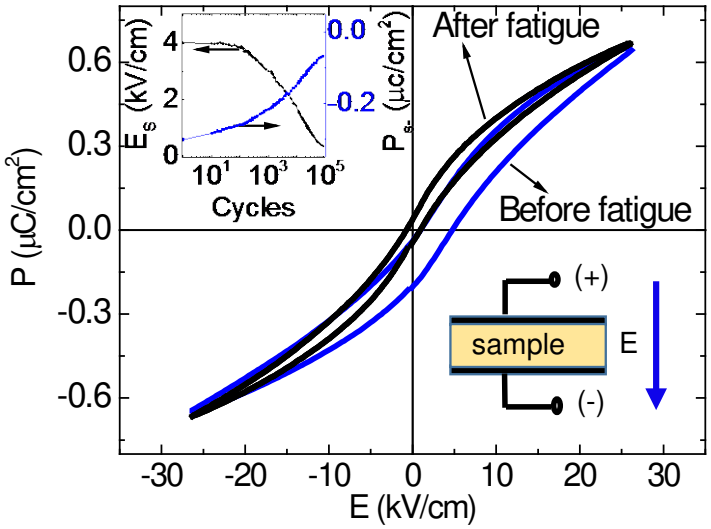

Figure S8 The polarization fatigue of the positively poled polarization state, the evolution of P-E loops before fatigue and after fatigue. Inset image is the mean switching electric field $E_S=(E_{S+}+E_{S-})/2$ and negative remnant polarization P_{r-} as a function of the cumulative number of cycles. Poling electric field was set to be 2.5 kV/cm at RT. It is found that the electric-field-cycling also benefits the recovery of the internal field and the P-E loop shifts back to the origin after the electric-field cycled over 10^5 times. This suggests that such an internal field built in Mg-doped rutile TiO_2 is metastable.

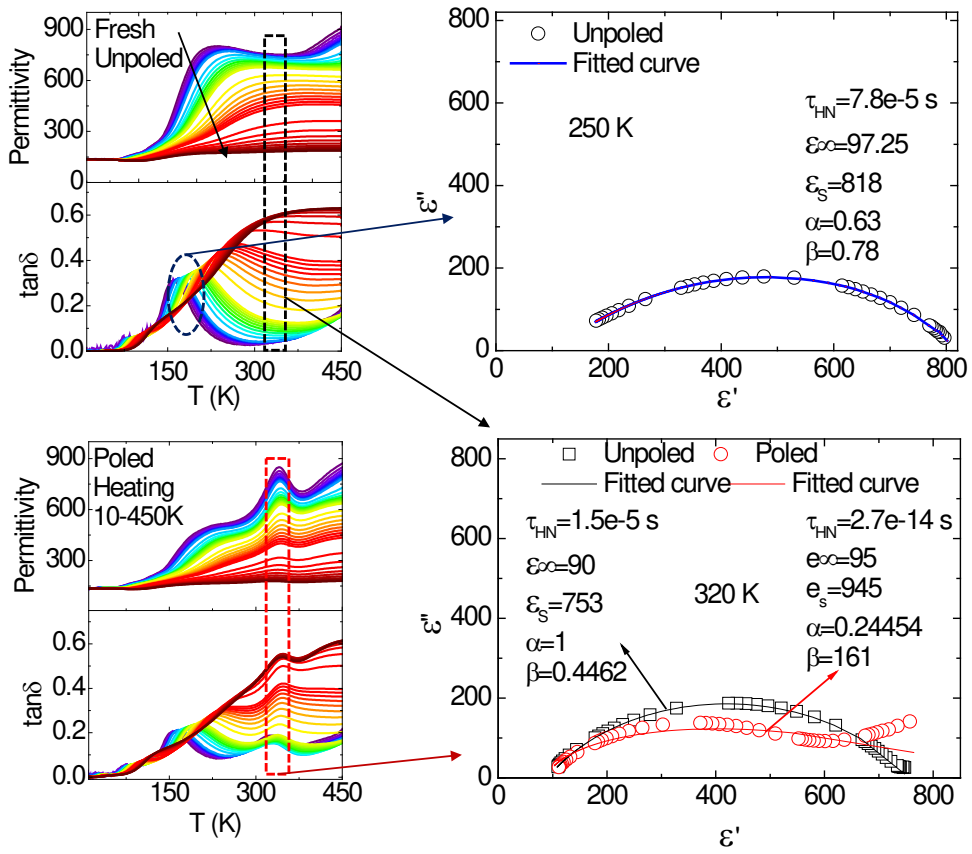

Figure S9 Temperature-dependent dielectric spectra of 0.25 at% Mg doped rutile TiO_2 for fresh sample (a) and poled sample (c) measured from 20 Hz to 1 MHz over the temperature range 10 K to 450 K. A negatively electric field of 2.5 kV/cm is applied for poling at room temperature. (b) The complex permittivity (ε^*) plot of 0.25 at% Mg doped rutile TiO_2 fitted with Debye-derivative Havriliak-Negami relaxation (HN) model[8] with respect to the relaxation peak just over 150 K. (d) The complex permittivity plot at selected temperature of 320 K for fresh sample (b) and with respect to the (d) as indicated by black and red dashed rectangle, respectively. The inset image in Figure S8b indicates an Arrhenius equation fitting on the thermal activated dielectric relaxation peak over 150 K corresponds to the blue dash circle in Figure S8a.

In the Debye-derivative Havriliak-Negami (HN) model,[8] the $\varepsilon^*(\omega)$ can be expressed in a general form:

$$\varepsilon^*(\omega) = \varepsilon_\infty + \frac{\varepsilon_s - \varepsilon_\infty}{(1+(i\omega\tau_{HN})^\alpha)^\beta} \quad (1)$$

where ε_s is the static permittivity, ε_∞ the permittivity in the high frequency limit, ω the frequency, τ_{HN} the relaxation time, α the parameter for the peak breadth of the distribution of relaxation frequency and β the parameter for the symmetricity of the distributed function. Equation (1) reduces to an original Debye model when $\alpha = \beta = 1$. The equation also reduced to Cole-Davison equation when $\alpha = 1$ and $0 < \beta < 1$.

It is obvious that the dielectric relaxation for the unpoled samples (Figure S9a) can be easily fitted quite well using Debye-like HN model with reasonable parameters (Figure S9b and Figure S8d), and the relaxation peak over 150 K and around 250 K was also analyzed by Arrhenius type fitting on f vs T to obtain an activation energy of 0.196 eV as shown in the inset image in Figure S8b. In contrast, the relaxation for the poled samples (Figure S9c) cannot be fitted by the Debye-like relaxation model as shown in Figure S9d, in which both the large value of relaxation time and value of β are non-physical.

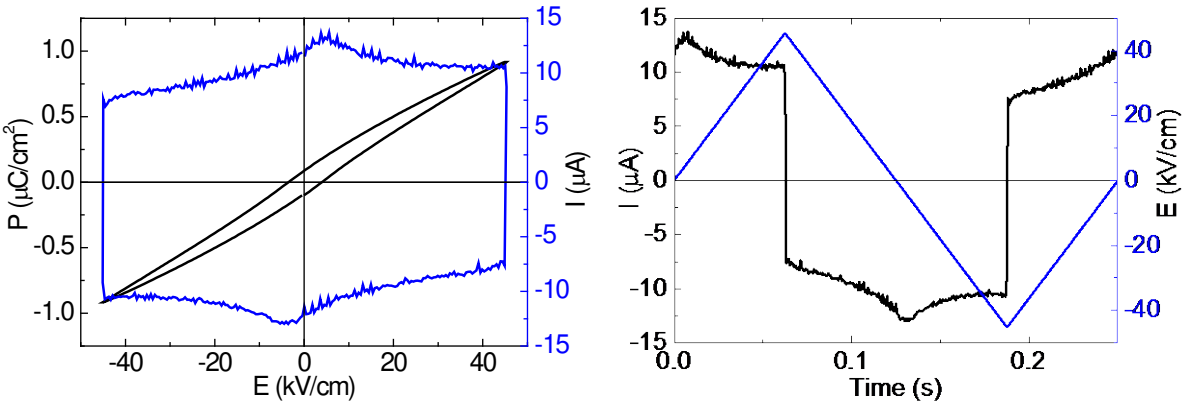

Figure S10 (a)-(b) Non-linear polarization behavior in 0.25 at% Ni-doped rutile TiO_2. P-E and I-E loops measured using a triangle wave method with an ac field of 4 Hz for 0.5 at% Ni-doped rutile TiO_2. Though the non-linear polarization behavior is not as obvious as that observed in Mg-doped rutile TiO_2 as shown in the main article, it is confirmed from the I-E loop where similarly two current peaks observed which is attributed to domain-switching-like behavior. For the current as a function of time, it is obvious that the current reaches a maximum when the voltage is close to zero, which is significantly different from that observed in linear dielectric behavior like in pure rutile TiO_2 where the current is only proportional to the change of the voltage.

II. Model used to fit the additional thermal activated dielectric relaxation

The model was developed as proposed by Macedo et al.[9] This model considers the relaxation act as the occurrence of two simultaneous events:

First, the molecule must attain sufficient energy to break away from its neighbors and change its orientation. Second, there must be a site with a defect in the vicinity of the moving molecule with sufficient local free volume for reorientation to occur. The probability of a transition from one orientation of the molecule to another is given by:

$$P=P_aP_d \tag{2}$$

where P_a is the probability of attaining sufficient energy to break the bonds and P_d is the probability that there is defect, i.e. oxygen vacancy moves to facilitate the reorientation of defect dipoles.

The probability P_a can be calculated on the basis of the activation energy theory of Eyring.[10] In the modified form, it reads:

$$P_a \cong \exp[-E_a/k_B(T-T_0)] \tag{3}$$

where E_a the activation energy, k_B the Boltzmann constant, T_0 is called ideal glass temperature.

P_d can be described within the framework of the Cohen and Turnbull approach.[11] In this approach, P_d can be calculated as the probability of finding the volume V^* of a defect necessary for a molecule reorientation to occur and is given by

$$P_d \cong \exp(-V^*N/V) \tag{4}$$

where V is the average free volume per defect. One should bear in mind that the value of the volume V^* is close to the volume of the molecule volume. The free volume concept deals with a constant number of molecules and considers the temperature dependences of the free volume. We assume that the temperature dependences of the number of defects N can be described by Boltzmann's law:

$$N=N_0 \exp(-E_d/k_BT) \tag{5}$$

where N_0 is the average number of reorientational molecules in the matrix, and E_d is the energy of the defect formation. By substitution Equation (3) to Equation (2) and taking into account that the V varies with temperature as a linear function, i.e. far less than the exponential term, we obtain

$$P_d \cong \exp(-C\exp(-E_d/k_BT)) \quad (6)$$

where $C=V^*N/V$. According to the definition, V^*/V stands for the maximum possible number of defects in the matrix. Therefore, C is a constant and is related to the defect concentration, and in the current case proportional to the capacitance of the measuring capacitor cell.

Assuming the dipole relaxation frequency is proportional to the transition probability, the relaxation frequency is obtained by

$$f = f_0 \exp[\frac{E_a}{k_B(T-T_0)} + C\exp(-\frac{E_d}{k_BT})]^{-1} \quad (7)$$

which describe the temperature dependences of the relaxation time corresponding to the relaxation process with simultaneous events of dipole reorientation and defect formation.

In our case, we treat the lattice polarization as the "reorienting molecule", with the defect transformation via oxygen vacancy movement taking the place of opening defects in the original theory. This facilitates alignment/de-alignment of defect-dipoles. E_a corresponds to the reorientation of the lattice in response to a defect transformation, and E_d corresponds to defect transformation (oxygen-vacancy move) during the alignment/de-alignment of defect-dipoles. The thermal activated behavior demonstrated in the frequency depend relaxation due to electrical poling was analyzed based on Equation (7). The best fitting gives reasonable parameters as follows: f_0=1.91×10^{12} Hz, E_a=0.0438 eV, E_d=1.6 eV, T_0=321.47 K, and C=2.5×10^{10}. One should note, the E_d calculated here is within the mean activation energy range calculated by the DFT where both the equatorial position (four equilibrium sites) and axial position (two equilibrium sites) can be the site of the vacancy with different energy barriers between them (1.26 eV for equatorial position, and 1.77 eV for axial position). Therefore, the experimental results are quite consistent with the DFT calculation results.

We also further modified the fitting model by considering the different defect transformation energies. Following Equation (6), the temperature dependences of the number of defects N can be divided into two parts by $N=N_1+N_2$ where N_1 and N_2 corresponds to equatorial and axial position, respectively. Therefore, N can be written as:

$$N=N_{01}\exp(-E_{d1}/k_BT)+N_{02}\exp(-E_{d2}/k_BT) \quad (8)$$

where N_{01} and N_{02} are the average numbers of the two types of reorientational defect-dipoles corresponds to the two kinds of oxygen vacancy occupations, respectively, and their corresponding defect formation energy are E_{d1} and E_d, respectively. By substitution Equation (3) in to Equation (2) and taking into account that the V varies with temperature as a linear function, i.e. far less than the exponential term, we obtain

$$P_d \cong \exp[-C_1 \exp(-E_{d1}/k_B T) + C_2 \exp((-E_{d2}/k_B T)] \quad (9)$$

where C_1 and C_2 are defect concentrations corresponds to the two type of oxygen vacancy occupations.

Therefore, Equation (7) is modified as

$$f = f_0 \exp[\frac{E_a}{k_B(T - T_0)} + C1\exp(-\frac{E_{d1}}{k_B T}) + C2\exp(-\frac{E_{d2}}{k_B T})]^{-1} \quad (10)$$

The poling induced relaxation process was analyzed based on both Equation (7) and Equation (10) as shown in Table S1. The best fitting results by equation (10) are shown in Figure 2e in the text.

Table S1: The parameters obtained from best fitting the experimental data using Equation (7) and Equation (10).

	f_0 (Hz)	E_a (eV)	E_d (eV)	E_{d1} (eV)	E_{d2} (eV)	T_0 (K)	χ^2
Equation (7)	1.91×10^{12}	0.0438	1.6	--	--	321.469	788.91
Equation (10)	2.64×10^{12}	0.0435	--	1.26	1.769	321.58	668.99

Both equations can give a good fitting with reasonable fitting parameters. By fitting using Equation (7) we obtained a mean energy ~1.6 eV for defect formation, while using Equation (10) leads to slightly better fitting results with two activation energies of 1.26 eV and 1.77 eV, which are consistent with the results calculated by DFT of 1.3 eV and 1.8 eV, respectively. All the parameters are reasonable within the framework of ionic polarization[12] The eigen frequency is around 10^{12} Hz, which is within the THz range and reasonable for general ionic displacement. T_0 is quite close to the temperature corresponding to the relaxation peak ~328 K measured at 100 Hz. The relaxation behavior on the basis of the simple model developed is thus very consistent with the theoretical calculation results and other data. The dielectric relaxation analysis based on this model and

theoretical calculation providing robust evidence for the nonlinear polarization behavior and abnormal electric polarization. The model can be applied to the interpretation of the dynamic of defect-dipole distributed in the metal oxides.

References

1. S. K. B. Srivastava, M.; Brahma, B.; Bouzerar, G., *Cond. Matter Mater. Sci.*, 2015, **arXiv preprint arXiv:1510.04782**.
2. J. Wang, M. Qin, H. Tao, W. Ke, Z. Chen, J. Wan, P. Qin, L. Xiong, H. Lei, H. Yu and G. Fang, *Appl. Phys. Lett.*, 2015, **106**, 121104.
3. *The bond valence approach at http://kristall.uni-mki.gwdg.de/softbv/ (Date of acess: 09/10/2016).*
4. W. Dong, W. Hu, T. J. Frankcombe, D. Chen, C. Zhou, Z. Fu, L. Cândido, G. Hai, H. Chen, Y. Li, R. L. Withers and Y. Liu, *J. Mater. Chem. A*, 2017, **5**, 5436-5441.
5. J. Zhuang, S. Weng, W. Dai, P. Liu and Q. Liu, *J. Phys. Chem. C*, 2012, **116**, 25354-25361.
6. V. Ischenko, S. Polarz, D. Grote, V. Stavarache, K. Fink and M. Driess, *Adv. Funct. Mater.*, 2005, **15**, 1945-1954.
7. Q. Zhang, M. Xu, B. You, Q. Zhang, H. Yuan and K. Ostrikov, *Appl. Sci.*, 2018, **8**, 353.
8. S. Havriliak and S. Negami, *Polymer*, 1967, **8**, 161-210.
9. P. B. Macedo and T. A. Litovitz, *J. Chem. Phys.*, 1965, **42**, 245-256.
10. S. Glasstone, K. J. Laidler and H. Eyring, *The theory of rate processes; the kinetics of chemical reactions, viscosity, diffusion and electrochemical phenomena*, McGraw-Hill Book Company, 1941.
11. D. Turnbull and M. H. Cohen, *J. Chem. Phys.*, 1961, **34**, 120-125.
12. A. K. Jonscher, *Chelsea Dielectrics Press.*, 1996.